Applications of ArcticDEM for measuring volcanic dynamics, landslides, retrogressive thaw slumps, snowdrifts, and vegetation heights

Chunli Dai [a,*], Ian M. Howat [b], Jurjen van der Sluijs [c], Anna K. Liljedahl [d], Bretwood Higman [e], Jeffrey T. Freymueller [f], Melissa K. Ward Jones [g], Steven V. Kokelj [j], Julia Boike [h,i], Branden Walker [k], Philip Marsh [k]

[a] *School of Forest, Fisheries,and Geomatics Sciences (FFGS), University of Florida, Gainesville, FL, USA*
[b] *Byrd Polar and Climate Research Center, The Ohio State University, Columbus, OH, USA*
[c] *Northwest Territories Centre for Geomatics, Government of Northwest Territories, Yellowknife, NT, X1A 2L9, Canada*
[d] *Woodwell Climate Research Center, Falmouth, MA, USA*
[e] *Ground Truth Alaska, Seldovia, AK, USA*
[f] *Department of Earth and Environmental Sciences, Michigan State University, East Lansing, MI, USA*
[g] *Water and Environmental Research Center, University of Alaska Fairbanks, Fairbanks, AK, USA*
[h] *Permafrost Research Section, Alfred Wegener Institute Helmholtz Centre for Polar and Marine Research, Potsdam, Germany*
[i] *Geography Department, Humboldt-Universität zu Berlin, Berlin, Germany*
[j] *Northwest Territories Geological Survey, Department of Industry, Tourism and Investment, Government of Northwest Territories, Yellowknife, NWT, X1A 2L9, Canada*
[k] *Cold Regions Research Centre, Wilfrid Laurier University, Waterloo, ON, N2L 3C5, Canada*

ABSTRACT

Topographical changes are of fundamental interest to a wide range of Arctic science disciplines faced with the need to anticipate, monitor, and respond to the effects of climate change, including geohazard management, glaciology, hydrology, permafrost, and ecology. This study demonstrates several geomorphological, cryospheric, and biophysical applications of ArcticDEM – a large collection of publicly available, time-dependent digital elevation models (DEMs) of the Arctic. Our study illustrates ArcticDEM's applicability across different disciplines and five orders of magnitude of elevation derivatives, including measuring volcanic lava flows, ice cauldrons, post-failure landslides, retrogressive thaw slumps, snowdrifts, and tundra vegetation heights. We quantified surface elevation changes in different geological settings and conditions using the time series of ArcticDEM. Following the 2014–2015 Bárðarbunga eruption in Iceland, ArcticDEM analysis mapped the lava flow field, and revealed the post-eruptive ice flows and ice cauldron dynamics. The total dense-rock equivalent (DRE) volume of lava flows is estimated to be (1431 ± 2) million m^3. Then, we present the aftermath of a landslide in Kinnikinnick, Alaska, yielding a total landslide volume of $(400 \pm 8) \times 10^3 \, m^3$ and a total area of $0.025 \, km^2$. ArcticDEM is further proven useful for studying retrogressive thaw slumps (RTS). The ArcticDEM-mapped RTS profile is validated by ICESat-2 and drone photogrammetry resulting in a standard deviation of 0.5 m. Volume estimates for lake-side and hillslope RTSs range between $40,000 \pm 9000 \, m^3$ and $1,160,000 \pm 85,000 \, m^3$, highlighting applicability across a range of RTS magnitudes. A case study for mapping tundra snow demonstrates ArcticDEM's potential for identifying high-accumulation, late-lying snow areas. The approach proves effective in quantifying relative snow accumulation rather than absolute values (standard deviation of 0.25 m, bias of -0.41 m, and a correlation coefficient of 0.69 with snow depth estimated by unmanned aerial systems photogrammetry). Furthermore, ArcticDEM data show its feasibility for estimating tundra vegetation heights with a standard deviation of 0.3 m (no bias) and a correlation up to 0.8 compared to the light detection and ranging (LiDAR). The demonstrated capabilities of ArcticDEM will pave the way for the broad and pan-Arctic use of this new data source for many disciplines, especially when combined with other imagery products. The wide range of signals embedded in ArcticDEM underscores the potential challenges in deciphering signals in regions affected by various geological processes and environmental influences.

1. Introduction

In recent decades, the Arctic has experienced accelerated warming than the global average (e.g., Rantanen et al., 2022). It is a key region for quantifying the impacts of climate change on environmental processes. However, the Arctic is remote with often difficult field and airborne data acquisitions (e.g., Mallory et al., 2018; Van der Sluijs et al., 2018), which results in monitoring biases where observed patterns are limited to only a few permanent research stations, as well as temporal offsets in documenting events and studying long-term processes (e.g., Rixen et al., 2022).

Over the past two decades, differencing of digital elevation models

(DEMs) obtained from satellite remote sensing has been increasingly used for measuring changes in topography (e.g., Farr et al., 2007; Krieger et al., 2007; Gardelle et al., 2012; Bagnardi et al., 2016; Grohmann, 2018; Antonova et al., 2019a,b). However, the wide range in spatial resolutions, and accuracies, along with incomplete coverage at high latitudes and restricted data access, has limited the applicability of satellite-based elevation data sources to only a few applications with relatively high-magnitude topographic changes in isolated locations. To support pan-Arctic monitoring of elevation-dependent geomorphological, cryospheric, and biophysical parameters, there is a genuine need for a consistent, high-resolution satellite-based elevation time series with complete Arctic coverage and applicability to processes with different magnitudes. ArcticDEM (Porter et al., 2022) is a new dataset that can fill these gaps and offer more frequent, pan-Arctic observations at a high enough resolution (2 m) to capture many of the processes associated with climate change-driven land surface change and hazards.

ArcticDEM provides open-access high-resolution (2 m) digital elevation models (DEMs) created from stereoscopic images acquired by Maxar (formerly DigitalGlobe) satellites, including WorldView-1 (since 2007), WorldView-2 (since 2009), WorldView-3 (since 2014), and GeoEye-1 (since 2008). ArcticDEM data are generated based on stereo-photogrammetry using the Surface Extraction from TIN-based Search-space Minimization (SETSM) developed by Noh and Howat (2015, 2017, 2019). Produced and maintained by the Polar Geospatial Center, ArcticDEM covers all land areas above 60° North and all of Greenland, Alaska, and Kamchatka. ArcticDEM includes two data products: ArcticDEM strips (Porter et al., 2022) and mosaics (Porter et al., 2023). ArcticDEM strips are time-dependent DEMs directly generated from stereoscopic images preserving the temporal component of image acquisitions, while ArcticDEM mosaics are DEMs mosaicked by taking the per-pixel median height value from the entire stack of DEM strips. This study mainly focuses on ArcticDEM strips, spanning the time frame from 2007 to 2022 as of the latest release (ArcticDEM strips version 4.1, Release October 2022). This new version (https://www.pgc.umn.edu/data/arcticdem/) includes 440,949 time-dependent strip DEM files, exceeding temporal densities of 7 strips for 84% of the ArcticDEM domain (Fig. 1), with more repeats over higher latitudes due to the

near-polar orbits of the Maxar satellites. The ArcticDEM strips version 4.1 has 180,208 more strips and four more years of data compared to the previous version, the ArcticDEM version 3 strip data (Porter et al., 2018; Dai et al., 2020a). To reduce holes caused by excessive filtering in the previous version, the DEM strips of the new version (4.1) preserve all data instead of applying the estimated error masks corresponding to clouds, shadows, detector saturation, water surfaces, and other sources. The error mask information is provided in separate auxiliary files. ArcticDEM represents Earth's surface elevation as a digital surface model (DSM), i.e., including the presence of vegetation, snow, and man-made structures, in contrast to a digital terrain model (DTM) which defines a bare-Earth model (e.g., Brovelli et al., 2004).

Since its first pan-Arctic release in 2018, ArcticDEM has been used for a wide range of applications, including measuring fluvial drainage patterns and hydrological changes (e.g., Dai et al., 2018; Lu et al., 2020), quantifying lava flows and deposits of volcano eruptions (Dai and Howat, 2017; Dai et al., 2020a, 2022), quantifying ice surfaces dynamics of glaciers and ice caps (e.g., Zheng et al., 2018; Durkin et al., 2019; Shean et al., 2019; Shiggins et al., 2023), and monitoring slow-moving landslides and retrogressive thaw slumps (e.g., Dai et al., 2020b; Corsa et al., 2022; van der Sluijs et al., 2023). Additionally, ArcticDEM-derived variables have been shown to improve the predictive power of biophysical attributes such as forest biomass (Puliti et al., 2020), land cover (Karlson et al., 2019), and more generally provide important context and basemaps to reconstruct Arctic deglaciation chronologies and glacial land systems (McMartin et al., 2021; Dulfer et al., 2023).

This paper is in response to the anticipation of increasing usage of ArcticDEM's time-dependent DEM strips data due to their pan-Arctic coverage, open data policy, and researchers' accessibility to high-performance computational resources. The upcoming global coverage of the time-dependent DEMs, such as EarthDEM and the reference elevation model of Antarctica (REMA, Howat et al., 2019), will further broaden their application to the global domain, largely increasing their impact on geosciences beyond the current ArcticDEM user base. Users from various backgrounds need detailed information on the error characteristics and behavior of ArcticDEM strips with linkages to specific applications. A broadened user base will also push applications
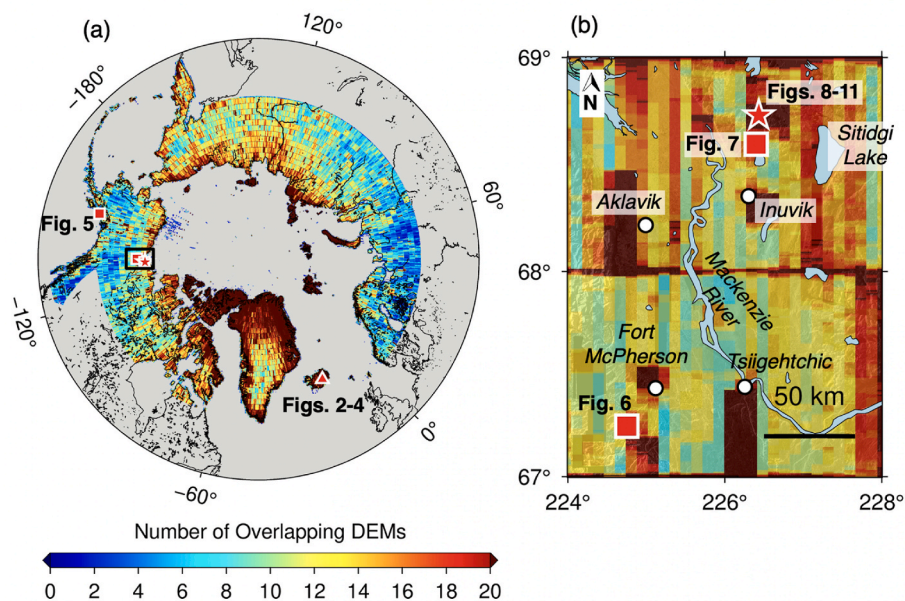

Fig. 1. ArcticDEM strip density (version 4.1, release Oct. 2022) and study areas. (a) The number of overlapping ArcticDEM strips over the entire Arctic. (b) A closer look at northwestern Canada (the black box in (a)). The red triangle denotes the Bárðarbunga volcano. Red squares show the locations of the Kinnikinnick landslide (Fig. 5) in Alaska and two thaw slumps in the Peel Plateau (Fig. 6) and near Inuvik (Fig. 7), Canada. The red star shows our snow and vegetation site in the Trail Valley Creek research watershed, Northwest Territories, Canada. (For interpretation of the references to color in this figure legend, the reader is referred to the Web version of this article.)

beyond monitoring phenomena at large magnitudes (e.g., large landslides, volcanic eruptions, large-scale glacier dynamics) to explore usage at lower expected magnitudes and signal-to-noise ratios. The time-dependent nature of strip DEM files and their increasingly improved temporal resolution will result in a shortening of the interval of change detection analysis, from single one-time observations to multi-temporal analyses between individual years or even months. Therefore, if error characteristics are sufficiently understood, current and future ArcticDEM releases have the potential to document events and Earth surface processes at higher fidelities and over greater spatial scales.

In this paper, we further demonstrate the applications of ArcticDEM in different disciplines and regions by (1) showing how the DEM time series analysis can aid in the detection and monitoring of topographic dynamics, (2) providing case study examples of Earth surface processes with mass change volumes spanning 5 orders of magnitude, from lava flows on the order of 10^9 m^3 to thaw slumps on the order of 10^4 m^3, and (3) illustrating common error characteristics that users will encounter in the pursuit of lower magnitude and or shorter time-interval change detection analyses. The case studies demonstrated in this paper will guide the extended use of this openly accessible dataset in many disciplines. Specifically, the application of ArcticDEM data is shown in the following case studies.

1. Measuring ice cauldrons dynamics and lava flow for the 2014–2015 Bárðarbunga eruption,
2. Quantifying the depletion area and volume of the 2017 Kinnikinnick landslide in Alaska,
3. Monitoring retrogressive thaw slumps in northwestern Canada, and
4. Measuring snowdrift variations and vegetation heights.

2. Methods

2.1. DEM coregistration

The internal (pixel-to-pixel) accuracy of ArcticDEM strips can reach up to 20 cm (Noh and Howat, 2015). However, DEM strips derived from stereophotogrammetry have systematic translational and rotational offsets (up to several meters) (Noh and Howat, 2013) caused by errors in the imaging sensor model. In order to retrieve actual topographic changes from DEM differencing, DEMs should first be precisely coregistered with each other or coregistered to more precise LiDAR elevations or ground control points (e.g., Noh and Howat, 2013; Li et al., 2023). The process of coregistration was carried out using a fast, simple, and robust coregistration method developed by Nuth and Kääb (2011). This adopted method demonstrates efficiency, producing coregistration results in minimal iterations due to its reliance on a comprehensive analytical solution for calculating a 3-D shift between DEMs, facilitated by elevation derivatives of slope and aspect. In situations where dynamic change areas are identifiable based on a priori information, such as the lava flow field surrounding the Bárðarbunga volcano or the glacier regions adjacent to the 2017 Kinnikinnick Landslide, we manually cropped out these areas to further enhance the reliability of DEM coregistration. Translational offsets for DEMs processed in this study are detailed in Tables S1–S3.

2.2. Mapping sudden surface changes

To estimate the sudden changes in topography due to, for example, a volcanic eruption, landslide, or retrogressive thaw slump, we adopt the time-series analysis of DEM strips based on least-squares adjustment as described in previous publications (e.g., Dai and Howat, 2017; Dai et al., 2020a, 2022). Here we briefly reiterate the methodology (e.g., Dai et al., 2022). The surface elevation time series from ArcticDEM measurements can be modeled using a constant value and a change of elevation using the Heaviside step function. We have

$$y = a + b \times H(t - t_e) \tag{1}$$

where y is the surface elevation (in meters) measured at acquisition time (t in years), and t_e (in years) is the time when the largest magnitude of change occurs. a is the constant surface elevation before the change in units of meters, b is the estimated magnitude of elevation change, in meters. $H(t - t_e)$ is the Heaviside step function as shown in Dai and Howat (2017). For temporally discrete landslides or volcanic eruptions, the time of change is normally adopted from known information, while for retrogressive thaw slumps (RTS), the time of change is considered at the time sequence during which the largest magnitude of surface elevation change occurred.

Parameter b is the desired quantity which is estimated through least-squares adjustment. In this simple linear fit model (Eq. (1)), the parameter b represents the difference between the mean surface elevations before and after the event. The uncertainties are calculated by first quantifying the estimated variance component, $\widehat{\sigma}_0^2$, and then propagating the errors to the estimated magnitude of elevation change. $\widehat{\sigma}_0^2$ can be calculated by the following equation:

$$\widehat{\sigma}_0^2 = \widetilde{e}^T P \widetilde{e} / (n - m) \tag{2}$$

where n is the total number of DEM measurements, m is the number of unknown parameters, which is 2 here (i.e., the elevation change, b, and the surface elevation before the change, a), $\widetilde{e}$ is the estimated error vector (n by 1) of all measurements, P is the weight matrix (n by n), which is a unit matrix by assuming equal weight for all measurements. The square root of the estimated variance component (i.e., standard deviation) represents the uncertainty of elevation measurements. Standard error propagation is then adopted to estimate the uncertainty of the estimated parameters (e.g., the elevation change).

For mapping surface elevation changes caused by temporally discrete landslides and volcanic eruptions, abrupt elevation changes can be estimated by comparing DEMs before and after a time-specific event (Eq. (1)). In contrast to time-specific events, retrogressive thaw slumps (RTS) are a type of permafrost landslide that develop in ice-rich permafrost terrain and represent chronic sites of thaw-driven erosion that modify slopes over months, years, and decades, wherein periods of stabilization, inactivity, and reactivation occur (Lacelle et al., 2015; Ward Jones et al., 2019; Kokelj et al., 2021; van der Sluijs et al., 2023). For RTS-type landslides, we select the event time for each pixel as the epoch when the largest magnitude of surface elevation changes occurred, and then adopt the same equation (Eq. 1) to estimate elevation changes. While this DEM time series analysis method is suitable for discrete events, where a step-change occurs between periods of stability, the elevation change from Eq. (1) may be basically the same as a DEM of Difference (DoD) created using one pair of pre-and post-event DEMs. This would not be the case for RTS-type landslides occurring in ground ice-rich permafrost environments. Volume estimates for RTS derived from Eq. (1) may therefore differ from conventional DoD products. In this study, we compared and validated the results of the ArcticDEM time series at three known locations of RTS in the northwestern Canadian Arctic (Kokelj et al., 2021; van der Sluijs et al., 2023).

2.3. Snowdrift mapping

In an effort to retrieve mass wasting signals above minimum noise thresholds, we encountered data noise in the DEM time series introduced by late-season snowdrifts (winter DEMs) and vegetation height changes (summer DEMs). We hence further demonstrate the capabilities of ArcticDEM for measuring snowdrift variations and vegetation heights. One common way to measure snow depth is to use the difference between a snow-surface DSM and a snow-free bare ground elevation model (e.g., a digital terrain model by light detection and ranging – LiDAR) (e.g., Harder et al., 2016; Marti et al., 2016; Walker et al., 2020). Here we

show that the snowdrift thickness (snow depth with regional mean removed) can be retrieved from ArcticDEM data directly without the need for a LiDAR DTM, through the use of the median of summer DEMs as the snow-free reference elevation model.

We adopt a August 22, 2018 LiDAR DTM (Lange et al., 2021, Text S1) as the reference DEM for coregistration. The coregistration is carried out over selected control points (e.g., Fig. S1), which are pixels with vegetation height less than 0.1 m (Anders et al., 2018; Lange et al., 2021) and with vegetation types such as dwarf shrub, tussock, and lichen (Grünberg and Boike, 2019). The control points are selected to mitigate the effects of tall vegetation. The translational offsets of all DEMs with respect to the LiDAR DTM are listed in Table S1, and all are within ±6 m.

After DEM coregistration, we computed the median DEM from all summer DEMs as the snow-free reference. One major benefit of using the summer median as the reference is to greatly expand opportunities to pursue snowdrift analyses throughout the Pan-Arctic without relying on airborne LiDAR data (which has limited coverage), and secondly, it can reduce the effect of variable vegetation heights on the calculation of snowdrift. Then, the snowdrift thickness for each 2 m raster cell is calculated as

$$hs = DSM_{snow} - DSM_{snow\text{-}free} \qquad (3)$$

where, *hs* is snowdrift thickness for each pixel, DSM_{snow} is the snow surface elevation from ArcticDEM strips (Table S1), and $DSM_{snow\text{-}free}$ is the elevation of the snow-free surface from the median of summer DEMs. The field measurements of snow depth from the closest weather station INUVIK (50 km south of our study area) in Canada are listed in Table S1 for corroboration purposes. As discussed later in Section 3.4, since DEM coregistration removes regional mean snow depth, our algorithm only reflects spatial variations of snow depth.

2.4. Vegetation heights mapping

Vegetation height can be measured by calculating the difference between a digital surface model of the vegetation canopy and a digital terrain model (i.e., a DSM representing bare ground) (e.g., Neigh et al., 2014; Puliti et al., 2020). For example, after DEM coregistration as described above, the vegetation height for each pixel is calculated as:

$$hv = DSM_{veg} - DSM_{veg\text{-}free} \qquad (4)$$

where, *hv* is vegetation height for each pixel, DSM_{veg} is the vegetation surface elevation from ArcticDEM strips (Table S1), and $DSM_{veg\text{-}free}$ is the elevation of the bare ground surface from LiDAR. In cases when LiDAR data are not available, it may be feasible to use qualified ArcticDEM strips acquired in winter seasons when leaves are shed and there is no snow cover as the bare ground DEM (Zhang and Liu, 2021). Here we use only summer ArcticDEM strips as vegetation-covered DEMs, DSM_{veg}. The LiDAR DTM collected by Alfred Wegener Institute (Lange et al., 2021, Text S1) on August 22, 2018 is adopted as the bare ground topographic surface, $DSM_{veg\text{-}free}$.

3. Results

3.1. Lava flow and ice cauldrons from the Bárðarbunga eruption (August 2014 to February 2015) in Iceland

The Bárðarbunga caldera, located at the northwest corner of the Vatnajökull ice cap, collapsed between August 29, 2014, and February 27, 2015, and produced the Holuhraun lava flow 48 km away (e.g., Sigmundsson et al., 2015; Gudmundsson et al., 2016). Here we demonstrate the application of ArcticDEM strips data in quantifying the lava flow thickness, post-eruptive caldera ice flows, and ice cauldrons. At the Holuhraun lava field, 48 km northeast of the Bárðarbunga caldera, a total of 5 pre-eruptive and 34 post-eruptive ArcticDEM DEMs were processed (Table S2) with coregistration carried out over the stable

surfaces outside the lava flow field and ice caps.

3.1.1. Lava flows

Fig. 2(b) shows the DEM time series near the main vent (Baugur vent, Witt et al., 2018), which yielded a lava thickness of 53 ± 1.2 m. The post-eruptive DEM strips data demonstrate a stable lava surface 4 years after the eruption. From the surface elevation change map (Fig. 2(c)), the lava flow area was delineated based on a minimum elevation increase of 2 m. The total estimated area of the lava flows in the Holuhraun plain is 86.2 km², slightly larger than the previous estimates (84.2 km²) from TanDEM-X data (Dirscherla and Rossi, 2018). Using the algorithms for estimating lava flow volume and uncertainty (Fig. S2, Bagnardi et al., 2016; Dai and Howat, 2017), the bulk volume was then calculated as $(1514 \pm 2) \times 10^6$ m³, consequently larger than the previous estimates $(1440 \pm 70) \times 10^6$ m³ by Dirscherla and Rossi (2018). Based on a lava density of 2600 kg/m³ and a basaltic magma density of 2750 kg/m³ (Gudmundsson et al., 2016; Dirscherla and Rossi, 2018), the bulk lava volume was converted to its dense-rock equivalent (DRE) of $(1431 \pm 2) \times 10^6$ m³. A few meters of subsidence in the southwest of lava flows (Fig. 2(c)) corresponds to the deflation of the lateral dykes (Sigmundsson et al., 2015), consistent with the graben structure discussed in Rossi et al. (2016).

3.1.2. Post-eruptive caldera ice flows

ArcticDEM data can also be used to recover the post-eruptive ice flow within the collapsed caldera. The ice surface experienced significant subsidence in 2016 in response to the caldera collapse, then it was slowly filled back in by snow accumulation and inflows of ice toward the center. As shown in Fig. 3, the DEM difference between October 14, 2016 and August 24, 2017 shows the ice surface rising at the center of the caldera and decreasing near the caldera rim, which is consistent with the ice flow distribution modeled in Gudmundsson et al. (2016). The post-eruptive ice surface change rate at the center of the caldera is around 6 m/year between 2016 and 2017. Fig. 3(b) shows the temporal changes along profile SN from four ArcticDEM strip data, as well as one pre-eruptive SPOT DEM (Korona et al., 2009).

3.1.3. Ice cauldrons

Furthermore, ArcticDEM data offers a low-cost and precise tool to map ice cauldrons, which are shallow ice depressions formed by magmatic heat or basal melting (e.g., Woods et al., 2018). As shown in Reynolds et al. (2017, 2019), ice cauldrons can be used as a calorimeter to explore the heat transfer mechanism in subglacial geothermal areas. Fig. 4 gives an example of quantifying ice cauldron volume from ArcticDEM differencing. For this ice cauldron (BB-03, named in Reynolds et al., 2019), the DEM difference between 2012 and 2017 represents the combination of the overall ice flow into the caldera and the local geothermal activity. The outline of this cauldron is retrieved by using a contour of −25 m to the DEM difference map, yielding a total area of 0.86 km². Geothermal activities were retrieved after bias removal (−17 m) due to background ice flows (similar to Reynolds et al., 2019), resulting in a total volume of 16 million m³. Reynolds et al. (2019) estimated a volume of 27 million m³ based on the interpolation of two airborne radar altimetry profiles (2011–2017). Their method required making assumptions about the geometry of the cauldron given elevation changes only from two crossing profiles, while our estimate is based on complete wall-to-wall stereo-photogrammetric data, that represents three-dimensional surfaces more reliably.

3.2. The 2017 Kinnikinnick Landslide in Alaska

In the late summer of 2017, satellite images showed a swath of dark rough material appearing on a small glacier near Upper Hazelle Lake in Kachemak Bay State Park, Alaska (herein referred to as the Kinnikinnick Landslide). The patch of rough material provides a brighter, noisier reflector, which can be seen in the Sentinel 1 reflectance images from 4
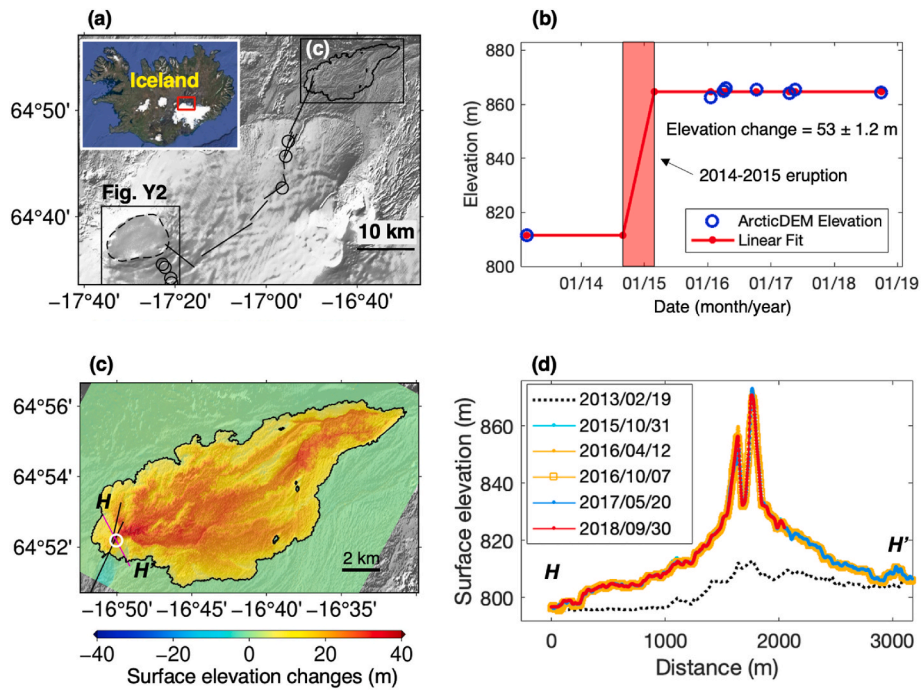
Fig. 2. The Holuhraun lava flow measured from ArcticDEM. (a) Hillshaded topography of the study area. The map is the hillshade of the ArcticDEM mosaic (Porter et al., 2023) created by the Polar Geospatial Center from DigitalGlobe, Inc. imagery. The black dashed line is the caldera rim, the black circles are ice cauldrons, and the black straight lines are dykes from Sigmundsson et al. (2015). Black boxes highlight the caldera and lava flow areas. The inset denotes the location of our study area. (b) ArcticDEM elevation time series and the linear fit (Eq. (1)) at the white circle in (c). (c) Lava flow thickness measured from ArcticDEM time series (Eq. (1)). (d) Topography profiles along HH'. The black dash line is the pre-eruptive topography. Colored lines are post-eruptive topography.
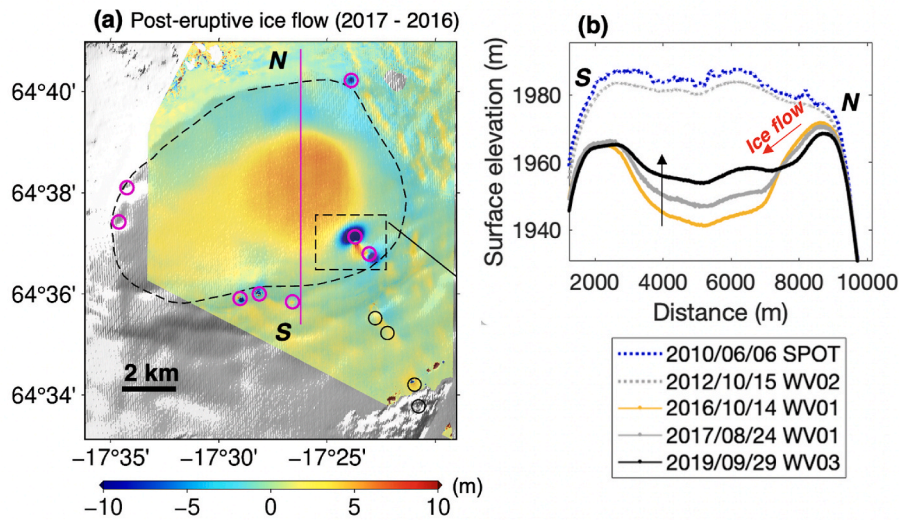

Fig. 3. Post-eruptive ice surface elevation changes at the Bárðarbunga caldera. (a) Post-eruptive ice flow in response to caldera collapse. Circles are ice cauldrons (Sigmundsson et al., 2015 (black); Reynolds et al., 2019 (purple)). The black box denotes the study area of Fig. 4. (b) Ice surface elevation profiles along **SN**. The abbreviation of satellites is added after the date, e.g., SPOT, WorldView-1 (WV01), WorldView-2 (WV02), and WorldView-3 (WV03). (For interpretation of the references to color in this figure legend, the reader is referred to the Web version of this article.)

September but not in the preceding image on 23 August (Fig. S3). Cloud cover prevented good imagery until a 19 October Landsat 8 image that clearly shows the deposit with a dusting of snow on it (Fig. S3).

Here we quantify the total area and volume of the landslide depletion zone by analyzing the DEM time series. Considering our study area is surrounded by glaciers (RGI Consortium, 2017) and to avoid the effect of glacier dynamics, we mapped out the glacier areas and only carried out DEM coregistration (Nuth and Kääb, 2011) over selected surfaces in the non-glaciated areas. We obtained three DEM strips prior to and one DEM

strip post the event (Table S3). The DEM time series analysis (Section 2) produced the 2D surface elevation change map (Fig. 5(a)), with surface elevation decreasing up to 40.2 ± 0.7 m (Fig. 5(d)). With a threshold of -2 m, the total volume of landslide material loss is $(400 \pm 8) \times 10^3$ m^3, and the total area is 0.025 km^2. This landslide modified the morphology of this mountain, shifting the ridge of the mountain southwards by about 34 m and reducing the summit by 20 m (Fig. 5(c)). The total area of the debris flow was estimated using imagery at 0.52 km^2, yet with an average debris thickness of 0.77 m (total volume of mass loss divided by
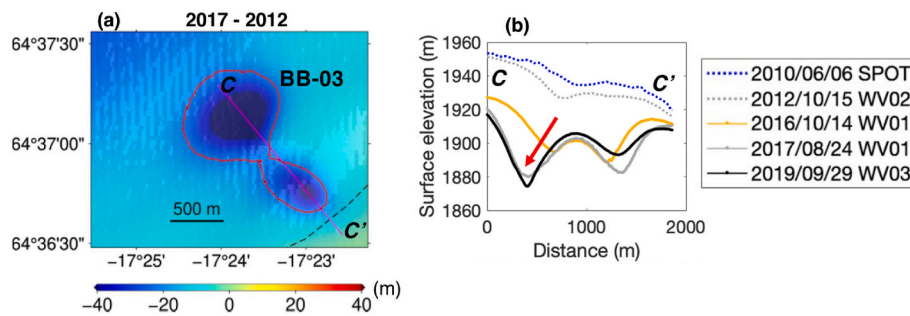
Fig. 4. Quantification of ice cauldron volumes. **(a)** Ice surface elevation changes between October 2012 and August 2017 ArcticDEM strips for the largest ice cauldron **BB-03** (name adopted from Reynolds et al., 2019). The outline of this cauldron is defined by the -25 m contour. **(b)** The ice surface elevations along profile CC'. The red arrow highlights how the ice cauldron moved from 2016 to 2019. (For interpretation of the references to color in this figure legend, the reader is referred to the Web version of this article.)
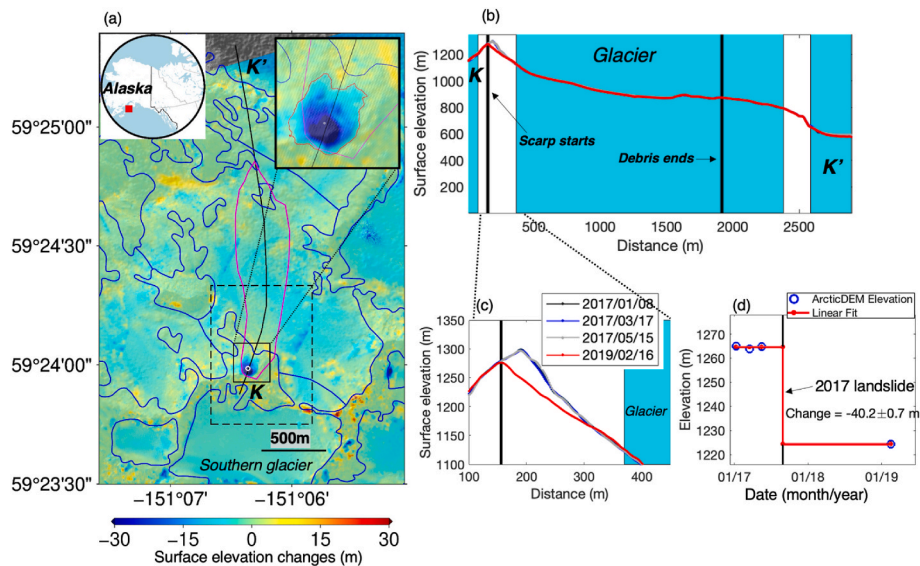

Fig. 5. Kinnikinnick landslide, Alaska. (a) Surface elevation changes. The background is the hillshade of ArcticDEM on January 8, 2017. The blue lines are glacier outlines from Randolph Glacier Inventory (RGI Consortium, 2017). The magenta polygon is the manually drawn landslide area from Landsat images (Fig. S3). The inset is the zoom-in near the scarp area, where the solid thin line highlights the scarp outline. The dashed rectangle denotes the boundary of Fig. S4. (b) Surface elevation profiles along KK'. The cyan bars highlight the profile sections that cross glaciers. The red line is the post-landslide topography, and other colors show pre-landslide topography. (c) The enlargement of (b) near the scarp area. (d) Surface elevation time series at the location of the white circle in (a). Blue circles are ArcticDEM measurements, and the red line is the linear fit. (For interpretation of the references to color in this figure legend, the reader is referred to the Web version of this article.)

the total area of the debris). The debris flow was not detectable from the DEM time series due to the high median uncertainty of elevation changes (1.6 m locally). In addition, since the debris spread out over the top of the adjacent glacier, the glacier melting signal overridden the small amount of thickening by debris flows.

Previous studies (Dai et al., 2020b; Corsa et al., 2022) have shown that DEM differencing from satellite optical imagery can reveal precursory ground motion before slope failures. By differencing the DEMs over different time intervals, we aim to search for pre-failure deformation similar to that observed at Barry Arm and Taan Fiord landslides. However, due to the snow cover in our target area (Fig. S4(d-f)), the surface elevation decrease around the mountain ridge (Fig. S4(b-c)) is likely dominated by snow depth variation (Brown and Brasnett, 2010). There was no detectable precursory deformation from the DEM differencing (Fig. S4(b-c)).

3.3. Retrogressive thaw slumps

One of the most noticeable topographic modifiers in the Arctic is retrogressive thaw slumping, which is a slope failure resulting from the thawing of ice-rich permafrost (Ward Jones et al., 2019; Kokelj et al., 2021; van der Sluijs et al., 2023). Here we demonstrate the use of the ArcticDEM time series at three long-term RTS study sites in the northwestern Canadian Arctic (e.g., van der Sluijs et al., 2023). Fig. 6(a) and Fig. 7 show the highest magnitude elevation change recorded for each pixel, which reveals the characteristic cuspate-shaped eroding scar area and elongated depositional debris tongue area of two thaw slumps in fluvial terrain (Lacelle et al., 2015, 2015, 2021; Kokelj et al., 2013; 2015; van der Sluijs et al., 2018), as well as a lake-side polycyclic thaw-slump (Kokelj et al., 2009) which are both parts of the NWT Geological Survey's long-term landslide monitoring and research program.

We validated ArcticDEM with ICESat-2 (ATL06) measurements (Smith et al., 2021) (snow-on data acquired on February 6, 2019) and a 1-m resolution drone-derived DEM (snow-free data acquired on September 25, 2019) (update of Van der Sluijs et al., 2018).The terms drones and unmanned aircraft systems (UAS) are used interchangeably in this paper. The topographic profiles (*TT'*) from ICESat-2 and ArcticDEM acquired one month later (March 10, 2019) agree well (Fig. 6(e)), with a standard deviation of 0.5 m (after removing the vertical bias of
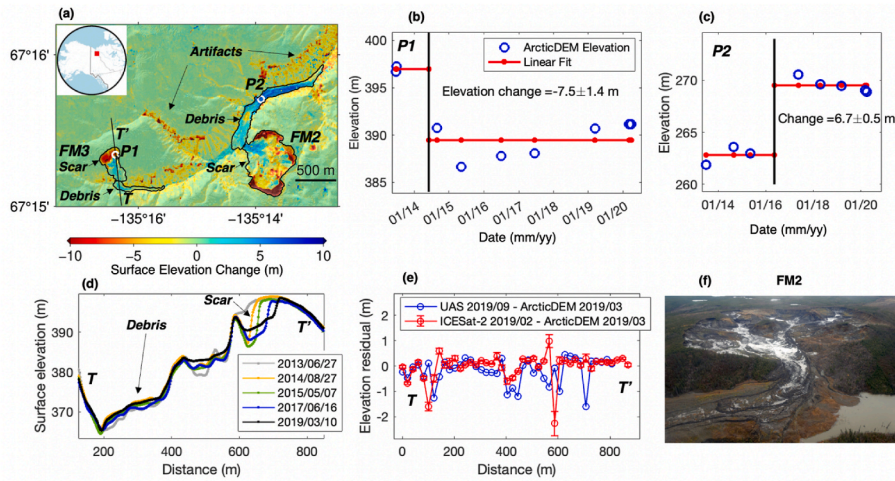
Fig. 6. Long-term thaw-slump monitoring sites (FM2 and FM3) in Peel Plateau, Canada. **(a)** Surface elevation changes from the ArcticDEM time series (Eq. (1)). The inset shows the location of our study area. The black outlines show the boundary of thaw slump scars and debris zones from image interpretation and field visits (Van der Sluijs et al., 2018). **(b)** Surface elevation time series at the white circle (P1) in the slump FM3 scar area. Blue circles are ArcticDEM measurements, and the red line is the linear fit. **(c)** Time series at P2 in the FM2 debris tongue area. **(d)** Selected topographic profiles from ArcticDEM illustrating headwall retreat and scar zone growth, as well as downslope mobilization of thawed materials. **(e)** Validation with ICESat-2 and drone data along the ICESat-2 ground track **TT'** (acquired on February 6, 2019). Red circles and error bars are ICESat-2 surface elevation differences with ArcticDEM (March 10, 2019) and uncertainties. **(f)** Oblique aerial photograph of the thaw slump FM2 (acquired September 19, 2020). Note that the blobs of red and yellow in (a) located on the steep yet stable slopes outside the delineated thaw slumps are often negative outliers and are artifacts of challenging ArcticDEM surface reconstructions at sharp valley crests covered in spruce forests and tall shrub vegetation (Kokelj et al., 2017). (For interpretation of the references to color in this figure legend, the reader is referred to the Web version of this article.)
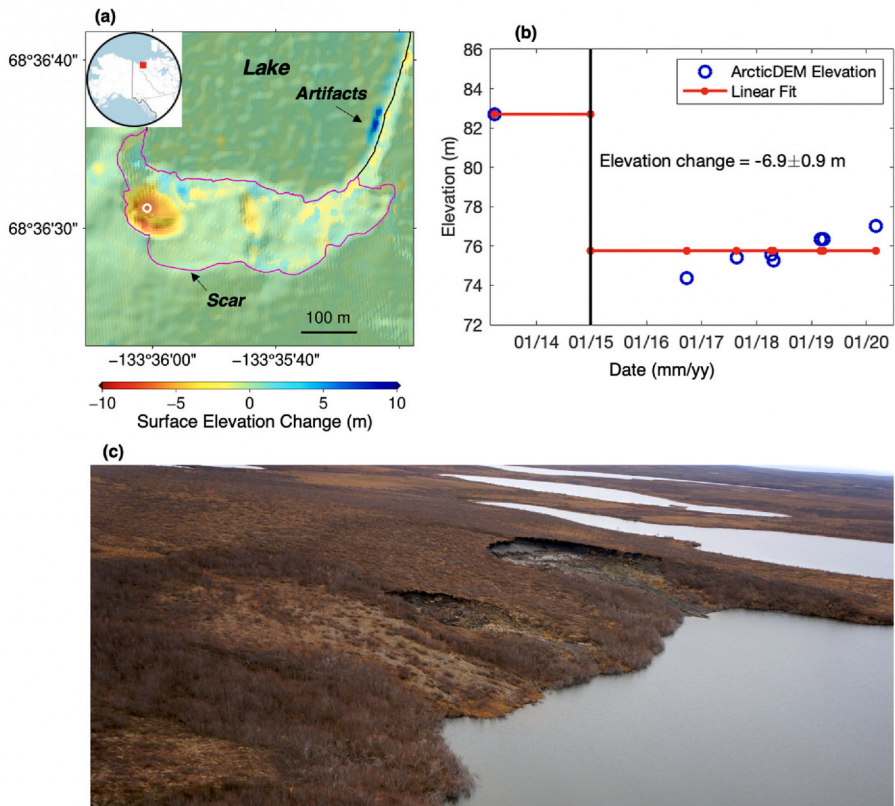

Fig. 7. Elevation changes at a lake-based slump (T4) in the Inuvik-Tuktoyaktuk region, Canada. (a) Surface elevation change map from ArcticDEM time series. The magenta outline shows the boundary of the thaw slump scar derived through image and field-based interpretation, and the black outline is the lake shoreline (Fig. 2 (c) in van der Sluijs et al., 2023). (b) ArcticDEM time series and the estimation of elevation change at the white circle in (a). (c) Oblique photograph of the thaw slump (acquired September 18, 2019). Note that the highly positive outlier in (a), such as those in blue near the lake edge, are sporadic artifacts. (For interpretation of the references to color in this figure legend, the reader is referred to the Web version of this article.)

2.2 m) and a high correlation coefficient of 0.998. Despite a snow effect, there is also good agreement between ArcticDEM and the drone DEM, with a standard deviation of 0.5 m along the profile (***FF'***) and a standard deviation of 0.9 m over the entire FM3 slump area (vertical bias of 4.6 m removed). The high accuracy of ArcticDEM enables the visualization of the yearly progress of headwall retreat as well as elevation decreases over the scar area (Fig. 6(d)). The results illustrate the close agreement in surface change observations between ArcticDEM and other elevation data sources, demonstrating that time-series of surface elevation from ArcticDEM are capable of capturing known geomorphic processes occurring on seasonal and annual time-scales that are otherwise difficult to measure.

It is worth reiterating that the ArcticDEM time series analysis provides the mean elevation difference before and after the epoch at the largest change for each pixel (Eq. (1)). This elevation change may differ from the simple difference between the first and last DEM that is more commonly used in geomorphology studies. For example, for the FM3 scar area (Fig. 6(b)), the largest elevation change derived from the DEM time series is overestimated when compared to the elevation change measurement between the first and last DEM. This is due to the challenge of representing complex RTS processes using linear model fits instead of piecewise or breakpoint analysis. Processes such as the accumulation of thawed material at the base of the headwall without subsequent downslope removal (i.e., the gradual infilling of material in the scar zone over time; Kokelj et al., 2021; Ward Jones and Pollard, 2021) first registers as a sharp elevation decrease followed by gradual elevation increases (Fig. 6(b)). In contrast, for the FM2 debris area the change derived from the DEM time series underestimates the surface elevation change observed between the first and last DEM (Fig. 6(c)). As thawed materials are eventually transferred downslope by gradual creep or episodic mass flow events, the debris tongue first increases in elevation and typically decreases afterward due to settling, compaction, and rill erosion (Kokelj et al., 2015, 2021; Van der Sluijs et al., 2018).

Since the volume estimates derived from the DEM time series (highlighting the largest change) may differ from conventional DoD products, we provide two volume estimates for each of the three RTSs based on: 1) a simple DoD between the first and the last ArcticDEM scenes, and 2) the change from DEM time series analysis (Eq. (1)). The volume estimates of scar zones at FM3 and T4 from the ArcticDEM time series are both larger than the ArcticDEM DoD method (Table 1). Nevertheless, the ArcticDEM-estimated volume gains using the simple DOD method for the FM2 debris tongue and the volume loss at lake-based RTS T4 were closer to observed DOD measurements using LiDAR and drone photogrammetry (Table 1). These results show that direct comparisons between different sensors and periods are challenging due to complex local controls and time-sensitive feedback mechanisms on RTS mass wasting (e.g., Zwieback et al., 2018, Tunnicliffe et al., in prep). For example, for slumps FM2 and FM3, the ArcticDEM-derived volume losses are underestimated using either method, which is likely due to the two years of difference in the measurement time span, as a major flow event was recorded in 2012 (Kokelj et al., 2015). In the absence of drone or LiDAR data, these challenges highlight the need for the increased spatial and temporal resolution that

ArcticDEM provides to study these complex sites.

3.4. Snowdrift in Trail Valley Creek, Canada

Snow depth in Arctic environments is characterized by high spatial heterogeneity caused by wind transport and deposition and follows topography and vegetation variations (e.g., Derksen et al., 2009). Thicker snow typically occurs in topographic troughs where blowing snow is deposited, while areas with shallow snow depths are usually found on topographic highs or open flat environments. Here we show how ArcticDEM time-series can be used to identify high snowdrift areas and reveal temporal patterns of snowdrifts, with observations in agreement with field data and drone photogrammetry at the Trail Valley Creek research site, near Inuvik, Northwest Territories, Canada (Walker et al., 2020). Snowdrift maps were retrieved from ArcticDEM by differencing snow-covered ArcticDEM strips (October, November, March, April, and May) against snow-free DEMs (ArcticDEM summer median or a LiDAR DTM). All ArcticDEM strips were coregistered to the August 22, 2018 LiDAR DTM (Lange et al., 2021). Coregistration reduced systematic offsets between DEM strips, but by doing so the mean snow depth in the study area was removed. Thus, rather than absolute snow depth measurements, the ArcticDEM strips are useful for measuring snowdrift variations and identifying high-accumulation, late-lying snow areas.

3.4.1. Validation of snowdrift measurements

As shown in Fig. 8, the snowdrift pattern derived from ArcticDEM data is similar to the snow depth map by Walker et al. (2020). The average bias between snow depth by Walker et al. (2020) and ArcticDEM-derived snowdrift thickness on April 22, 2018 is about −0.41 m, which might reflect the overall average snow depth that may have been artificially reduced due to DEM coregistration. The bias is close to the field snow depth on March 16, 2018 (0.49 m from the INUVIK weather station). Pearson's correlation (r) and standard deviation (σ) between snow depth maps by Walker et al. (2020) and ArcticDEM-derived snowdrift thickness were $r = 0.69$ and $\sigma = 0.25$ m. Note that the differences are not caused by the use of an old bare-ground DEM by Walker et al. (2020) as demonstrated in Fig. S5.

Using a LiDAR DTM as a snow-free surface, $r = 0.84$ and $\sigma = 0.27$ m and $r = 0.97$ and $\sigma = 0.11$ m, were achieved for snow depth validation profiles AA' and BB' (Fig. 9), respectively. Similar results were achieved when the median of five summer ArcticDEM strips (Fig. S7) was used as a snow-free surface, namely $r = 0.88$ and $\sigma = 0.23$ m and $r = 0.96$ and $\sigma = 0.14$ m, for profiles AA' and BB', respectively. Together these results indicate that ArcticDEM time-series can be used to identify high-accumulation, late-lying snow areas even if no LiDAR DTM is available as snow-free surface, which greatly expands opportunities for snowdrift analyses across the Pan-Arctic. Be aware that ArcticDEM is not suitable for measuring absolute snow depth in areas where snow distribution is uniform. For example, as expected, direct comparisons with the Magnaprobe field data yielded a low correlation ($r = 0.14$; Fig. 9(c)), caused by the overall low variation of the ArcticDEM signal along the transect (standard deviation of 0.13 m) and the removal of the mean snow depth in ArcticDEM.

Table 1
RTS volume estimates.

RTS	Volume (m^c)			Relative difference against ground truth (Drone)	
	ArcticDEM Simple DOD	DEM time-series	Drone - LiDAR[a] (2011–2019)	ArcticDEM Simple DOD	DEM time-series
FM3 scar zone [b] (2013–2020)	−102,000	−166,000 ± 16,000	−209,503	−51%	−21%
FM2 scar zone [b] (2013–2020)	−1,225,000	−1,160,000 ± 85,000	−1,886,000	−35%	−39%
FM2 debris tongue [b] (2013–2020)	+449,000	+356,000 ± 31,000	+443,983	+1%	−20%
T4 lake-based scar zone [c] (2013–2020)	−29,000	−40,000 ± 9000	−31,023	−7%	+29%

[a] Measured between 2011 (LiDAR) (Text S1) and 2019 (drone); update of Van der Sluijs et al. (2018).
[b] ArcticDEM dates: June 27, 2013–March 27, 2020.
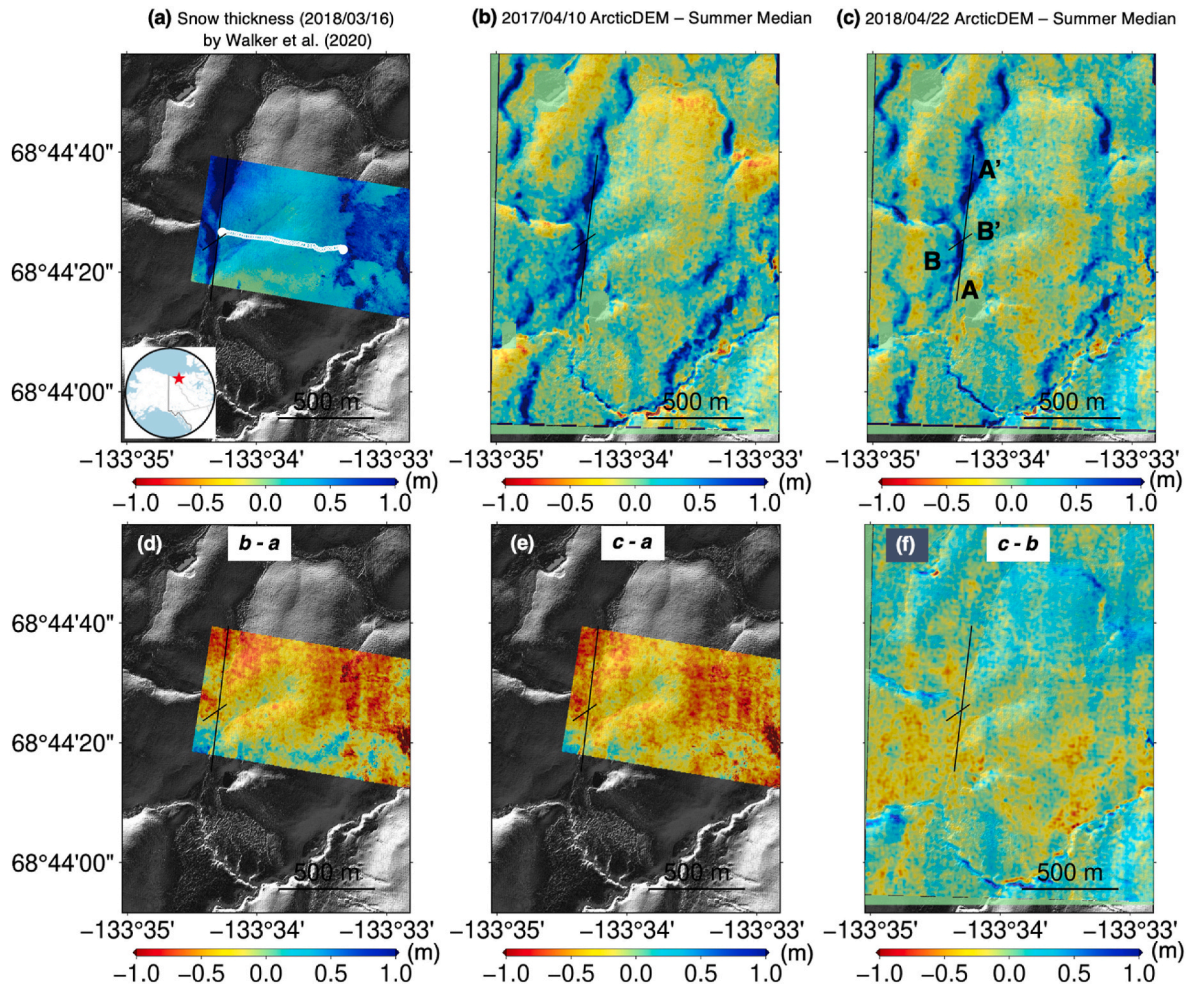[c] ArcticDEM dates: March 24, 2013–March 2, 2020.

Fig. 8. Snowdrift maps from ArcticDEM in Trail Valley Creek Research Watershed, Northwest Territories, Canada. **(a)** Snow depth on March 16, 2018 from Walker et al. (2020); 2020b). The study area is the area of interest (AOI) 7 in Walker et al. (2020). The inset shows the location of AOI7. White dots represent the field snow depth data measured by GPS Magnaprobe in Walker et al. (2020). **(b)** and **(c)** ArcticDEM derived snowdrift on April 10, 2017 and April 22, 2018. The snowdrift thickness is derived by subtracting the median of five ArcticDEM DEMs in the summer (see Fig. S7) from the winter DEMs. The background is the hillshade of the August 22, 2018 LiDAR DTM (Lange et al., 2021). **(d–f)** The snowdrift differences among the above three maps.

Note that our method shows negative snow thickness values in some areas because the mean snow depth was removed during coregistration, whereas Walker et al. (2020) manually set negative pixels to zeros. Comparing profile AA' between March 16 and April 22 (Fig. 9(a)), we notice that the snow melt near A′ is about 30 cm more than the melt at the middle of the profile. It's possible that the melt is faster at higher ground (88 m vs 84 m). The spatial pattern of the snow depth difference (Fig. 8(e and f)) does not indicate any systematic tilting. Nevertheless, the difference in snowmelt is negligible, which is almost near the uncertainty level of ArcticDEM data.

3.4.2. Temporal behavior of snowdrifts

The ArcticDEM strips can reveal the temporal dynamics of snowdrifts on annual and monthly scales. The similar pattern of snowdrift thickness in April 2017 (Fig. 8(b)) and 2018 (Fig. 8(c)) shows that snowdrifts in this area occur in the same locations from year to year. Comparing monthly observations, snowdrifts along profile AA' are not significant in October and November when snow accumulation remains small in the region (Fig. 10, Inuvik weather station: 0.04 m–0.2 m). Although the absolute ground snow depth was thickest (0.6 m) in March, the snowdrift signal (two peaks along profile AA', mean snow depth removed) was not significant, only around 0.5 m. The snowdrift signal reached the highest value, up to 1.5 m, in April, even though the absolute ground snow depth was slightly reduced (0.5 m). Along with the rapid melting

in May (absolute ground snow depth of only 0.1 m), the snowdrift signal was reduced to 1.3 m in May (blue line). The Worldview-2 satellite image (Fig. S8) validates the overall snow melt in late May and early June, and the coverage of snowdrift near the AA' section and other areas.

3.5. Vegetation heights in Trail Valley Creek, Canada

Previous studies have shown the feasibility of ArcticDEM DSMs in estimating canopy heights in different regions, such as Alaska (Meddens et al., 2018; Montesano et al., 2019; Zhang and Liu, 2021), the contiguous United States (Neigh et al., 2014), Norway (Puliti et al., 2020). Yin et al. (2023a, 2023b) evaluated the impacts of convergence angle, image resolution, and solar zenith angle on DSM-derived vegetation heights. This study further demonstrates the estimation and evaluation of vegetation heights in a unique tundra environment from ArcticDEM DSMs. The study area is the Arctic site of Trail Valley Creek, Northwest Territories, Canada. Maps of vegetation height are generated using summer snow-free ArcticDEM strips and a LiDAR DTM on August 22, 2018 as the bare ground surface (Eq. (4)). Comparisons across a tundra riparian stream valley (Fig. 11) showed the agreement between the LiDAR-derived vegetation height models (2016/09/13, 2018/08/22) and two ArcticDEM-derived vegetation maps. To obtain a baseline estimate of consistency in vegetation height estimates in the study area,
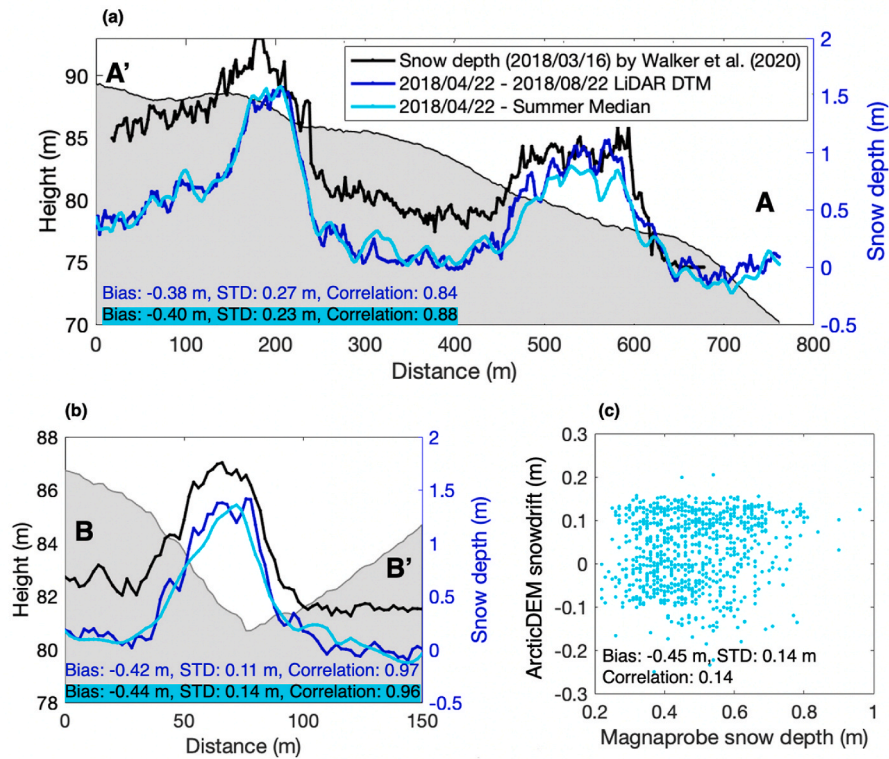
Fig. 9. Snowdrift validation along profiles. (a) Comparison along profile AA'. The black line denotes the snow depth on March 16, 2018 from drone photogrammetry in Walker et al. (2020). The blue and cyan lines show the snowdrift thickness from ArcticDEM on April 22, 2018 by subtracting the August 22, 2018 LiDAR DTM and the median of summer DEMs (Fig. S7), respectively. The gray shading represents the topography. (b) Comparison along profile BB'. (c) Scatter plot along points of GPS Magnaprobe measurements (white dots in Fig. 8(a)). The y-axis is the ArcticDEM-derived snowdrift thickness (April 22, 2018) with the summer median DEM as the bare-ground surface. The x-axis is the field snow depth measured using GPS Magnaprobe. (For interpretation of the references to color in this figure legend, the reader is referred to the Web version of this article.)
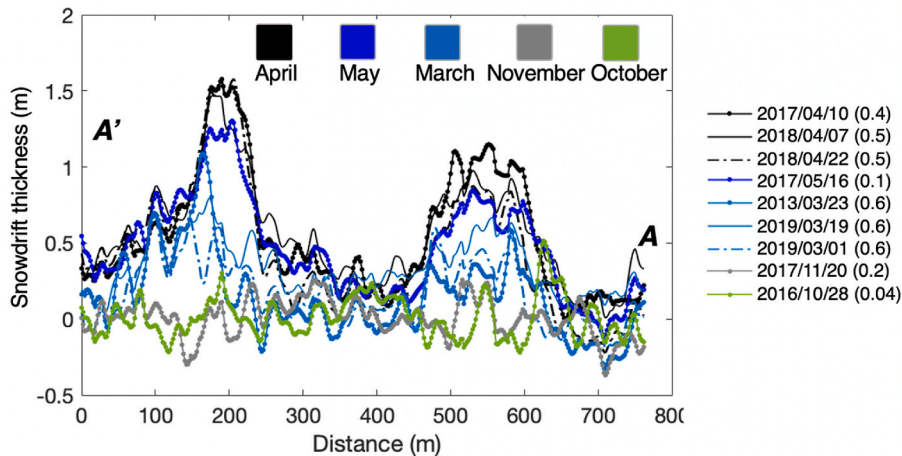

Fig. 10. ArcticDEM demonstrates temporal variability of snowdrifts. The profiles for each month are shown in the same color. The parenthesis shows the ground snow depth measurement (also in Table S1) from weather station INUVIK in meters. (For interpretation of the references to color in this figure legend, the reader is referred to the Web version of this article.)

the two LiDAR-derived vegetation height models show a bias of 0.08 m, standard deviation of 0.25 m and $r = 0.88$ along transect VV' (see Table 2). Measured against the 2016 LiDAR vegetation map (Anders et al., 2018), the observed biases (0.03 m–0.06 m), standard deviations (0.34 m and 0.33 m), and correlation coefficients ($r = 0.76$ and $r = 0.78$) indicated similar performance levels among vegetation heights derived from single ArcticDEM (2016/09/23, Fig. 11(b)) and summer-median ArcticDEM (Fig. 11(c)), respectively (see Table 2). The five summer

DSMs (Fig. S7) between 2015 and 2017 are selected for the calculation of summer median DSMs. The noticeable stripes from the individual ArcticDEM strip (Fig. 11(b)) are likely due to artifacts from imaging sensors (Shean et al., 2016), which are reduced in the summer median results (Fig. 11(c)). The negative vegetation heights from ArcticDEM are data errors (see section 4).

Comparisons between LiDAR and ArcticDEM-derived vegetation heights are carried out for six different vegetation types (Fig. S1a;
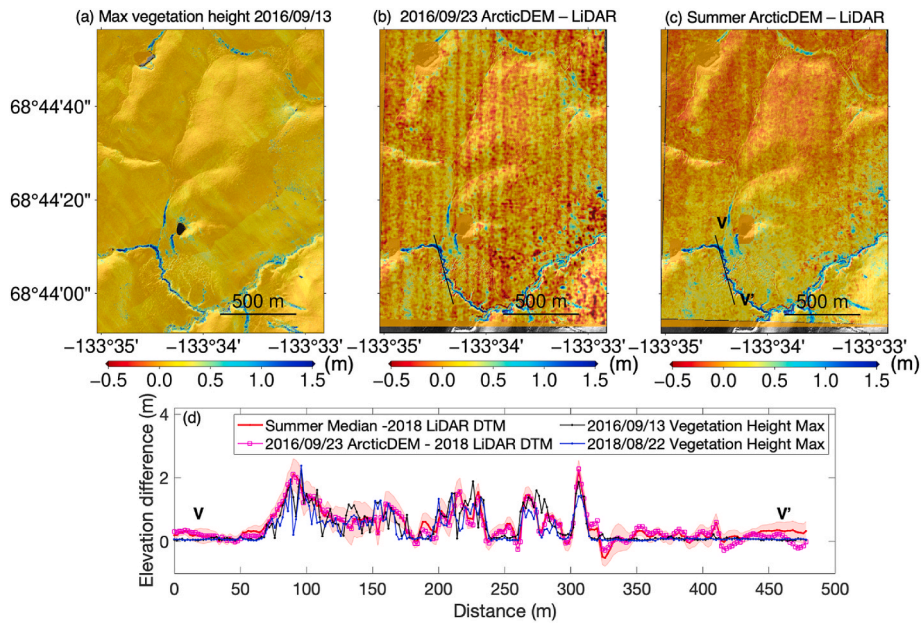
Fig. 11. Vegetation Height comparison along a tundra riparian stream in the Trail Valley Creek research watershed, Northwest Territories, Canada. (a) Maximum vegetation height map on September 13, 2016 from LiDAR data (Anders et al., 2018). (b) ArcticDEM-derived vegetation height from a single DEM strip (September 23, 2016), subtracting the LiDAR DTM on August 22, 2018. (c) ArcticDEM-derived vegetation height from the median of summer DEMs (Fig. S7) subtracting the LiDAR DTM (2018/08/22). All ArcticDEM DEMs are coregistered to the August 22, 2018 LiDAR DTM (Lange et al., 2021) using the control points in Fig. S1. (d) The vegetation height along profile VV'. The black, magenta, and red lines are profiles of (a), (b), and (c), respectively. The red shading denotes the uncertainty (around 0.3 m) from five ArcticDEM profiles (explained also in Fig. S7). The blue line is the maximum vegetation height from LiDAR on August 22, 2018 (Lange et al., 2021). (For interpretation of the references to color in this figure legend, the reader is referred to the Web version of this article.)

Table 2
Comparison of vegetation profiles along VV'.

	2018/08/22 LiDAR Vegetation	2016/09/23 ArcticDEM	ArcticDEM Summer Median
Bias	−0.08 m	0.03 m	0.06 m
STD	0.25 m	0.34 m	0.33 m
Correlation	0.88	0.76	0.78

Note: The reference vegetation height map is the maximum vegetation height on September 13, 2016 from LiDAR.

Grünberg et al., 2020; Grünberg and Boike, 2019). The correlation between these two data sets is strongest for tall vegetation (Table 3), e.g., the correlation is 0.8 for trees (height of 0.7 ± 0.9 m), and 0.6 for riparian shrubs (height of 0.3 ± 0.3 m). Correlations are weak (0.06–0.14) for all other short vegetation (dwarf shrub, tussock, lichen), e.g., mean height <0.3 m, which is below the threshold of ArcticDEM data for recovering surface elevation signal. The biases for all six types of vegetation are small (≤ 0.06 m) (see Table 3).

4. Discussion

4.1. Signal diversity in ArcticDEM hinges on geological environments

A broad range of signals can be retrieved from ArcticDEM data depending on geological settings. Here we validated the performance of ArcticDEM with existing publications, field measurements such as airborne LiDAR and UAS data, as well as ICESat-2 measurements. For example, the high resolution (2 m) of ArcticDEM produces a lava flow volume with uncertainty 35 times (2×10^6 m^3 compared to 70×10^6 m^3) better than the volume uncertainty from the 12 m resolution TanDEM-X data (Dirscherla and Rossi, 2018). The 2D coverage of ArcticDEM further supersedes airborne radar altimetry, which can only produce a rough estimation of ice cauldron volumes based on simple interpolation from a limited number of radar profiles (Reynolds et al., 2017, 2019).

With its pan-Arctic and extended temporal coverage, the ArcticDEM time series dataset provides a unique tool to capture the volumetric mass wasting dynamics of retrogressive thaw slumps. Here we demonstrated how the quantification of the largest sequential change in elevation time series can be linked to RTS form and evolution. The signals related to form and evolution may be exploited by image recognition in future

Table 3
Height comparison for different types of vegetation.

Types	2016 LiDAR Vegetation Height		ArcticDEM Vegetation Height (summer median)		Difference Between the 2016 LiDAR and ArcticDEM-Derived Vegetation Height			Total Area (m^2)
	Mean (m)	STD (m)	Mean (m)	STD (m)	Bias (m)	STD (m)	Correlation	
Tree	0.7	0.87	0.7	0.81	−0.02	0.5	0.8	13,540
Tall Shrub	0.16	0.1	0.17	0.2	0.01	0.2	0.11	472,622
Riparian Shrub	0.3	0.3	0.3	0.4	0.04	0.4	0.6	368,191
Dwarf Shrub	0.09	0.05	0.05	0.16	−0.04	0.2	0.14	997,368
Tussock	0.09	0.05	0.03	0.15	−0.06	0.2	0.06	1,038,466
Lichen	0.09	0.05	0.03	0.15	−0.06	0.2	0.06	368,646

Note: Here the ArcticDEM vegetation height is from the median of summer DEMs.

work toward the creation of a pan-Arctic mass wasting inventory using ArcticDEM (Nitze et al., 2021; Runge et al., 2022; van der Sluijs et al., 2023). ArcticDEM topographic profiles matched field-based drone surveys and ICESat-2 measurements well (standard deviation of around 0.5 m), and ArcticDEM profiles further illustrated how RTS evolves annually. ArcticDEM enables volumetric erosion and deposition estimates for a large population of thaw slumps, yet the method of retrieving only the greatest magnitude change for each pixel may obscure important RTS processes. For example, subsequent smaller elevation changes (both positive and negative) after thaw or deposition are averaged (Fig. 6(b and c)), so volume calculations may or may not be directly related to field conditions and the evolution of specific RTS. Furthermore, there are challenges with the use of winter DEMs, as snow biases volume changes and may lead to false positives when detecting RTS at regional scales from DEM datasets alone. Overall, the close agreement with the drone and airborne LiDAR (relative difference of around 20%) warrants more work using ArcticDEM strips for RTS inventories and volumetric analysis at a larger scale than what was previously possible due to the reliance on datasets with smaller geographic extents.

The snow and vegetation effects we encountered during investigations for geomorphological applications promote the exploration of ArcticDEM for detecting snowdrifts and vegetation heights. While the average snow depth over a study area is undesirably removed during DEM coregistration, ArcticDEM-derived snowdrift thickness maps can resolve the spatial heterogeneity of snow and identify the location of deep snowdrifts. We showed year-to-year consistency in the location of high-accumulation, late-lying snow areas in the Trail Valley Creek area, as well as the temporal dynamics of snow cover. ArcticDEM-derived snowdrift shows an uncertainty of around 0.25 m (up to 0.14 m for some profiles), which is comparable to the snow depth uncertainty of 0.15 m in Walker et al. (2020). The wider extent of ArcticDEM strips covers a typical area of 17 km wide and 110 km long, whereas the previous studies using UAS photogrammetry produced snow depth maps in relatively small areas (e.g., <3 km²) (e.g., Vander Jagt et al., 2015; Harder et al., 2016; Walker et al., 2020). Another advantage of ArcticDEM is that the data have been continuously collected by satellites since 2007 (Fig. 1), whereas UAS photogrammetry data are typically collected in field campaigns.

Moreover, our analyses highlighted the potential of ArcticDEM for estimating vegetation heights. Although in this study we used LiDAR data as the bare-ground terrain, it is possible to use an ArcticDEM from leaf-off scenes for retrieving independent vegetation heights in suitable scenarios as stated in Zhang and Liu (2021). Considering the relatively high uncertainties (0.33 m) of our ArcticDEM-derived vegetation heights, ArcticDEM performs better for tall vegetation, with a high correlation of 0.8 for trees (height of 0.7 ± 0.9 m) and a lower correlation of 0.6 for riparian shrubs (height of 0.3 ± 0.3 m) when compared with LiDAR results.

The illustrated five different applications from ArcticDEM imply the potential coupling of signals in areas with concurrent signal occurrences. For example, the inclusion of winter DEMs (with snow) will bias volumetric changes for RTSs and in many cases lead to data noise and outliers. The vegetation signal in ArcticDEM data may also cause challenges in retrieving landslide information. For example, as shown in Fig. 6(a), there are many artifacts along the steep valley crests that seem to be caused by vegetation height differences, instead of active slumping. Therefore, we foresee a need for the combined use of ArcticDEM strips, optical imagery, and supplementary datasets (e.g., surficial geology) to detect and monitor RTS at the regional to landscape scale.

4.2. Common error sources in ArcticDEM data

Together our case studies demonstrated common errors in ArcticDEM strips coming from different sources. First, there are large blunders caused by clouds, shadows, water bodies, as well as image saturation (Dai and Howat, 2018). These blunders can be mitigated through post-data processing, e.g., DEMs mosaicked using the median of multiple DEMs can mitigate outliers/clouds compared to the simple mean of DEM strips (Fig. S9). Second, there are small magnitudes of systematic errors, e.g., there might be a slight tilt (around 0.3 ± 0.03 m/km) in some ArcticDEM strips, which are most visible in DEM differences over relatively flat terrain (Fig. 11c–S10). The planar tilt in the satellite along-track direction (occasionally the cross-track direction) was also documented by Shean et al. (2016). In addition, DEM differences may also show periodical stripes (also called "jitter" artifacts) along the flight track direction (mostly north-south direction) as shown in the red patterns in (Fig. 11(b)), which are due to artifacts from imaging sensors (classified as detector sub-arrays boundary artifacts by Shean et al. (2016)). The wavelengths of these stripes vary from 64 m to 174 m with amplitudes around 0.05 m in our example (Fig. S11). Third, there are random DEM internal (pixel-to-pixel) errors, which are at the level of around 20 cm (Noh and Howat, 2015). And lastly, there are coregistration errors. As discussed in Section 2, translational offsets (e.g., Table S1) are systematic, and they can be evaluated using coregistration residuals, which vary around 0.5–2 m (Shean et al., 2016; Dai and Howat, 2017). Despite the numerous error sources, the demonstrated capabilities of ArcticDEM, including at lower magnitudes and near signal-to-noise ratios, will pave the way for a broad pan-Arctic use of this new data source in many scientific disciplines.

5. Conclusion

To support pan-Arctic monitoring, there is a need for consistent, high-resolution elevation time series with complete coverage and applicability to processes with different magnitudes. This study demonstrated ArcticDEM's wide range of applications for quantifying various Earth surface dynamics useful for geomorphological, cryospheric, and environmental biophysical disciplines. For volcanic eruptions, the ArcticDEM-derived lava flow field corresponding to the 2014–2015 Bárðarbunga eruption agrees with the previous publications while having a higher spatial resolution of 2 m. The lava flow's total dense-rock equivalent (DRE) volume is estimated to be (1431 ± 2) × 10^6 m³. In addition, ArcticDEM reveals the post-eruptive yearly changes in ice surface elevations at the Bárðarbunga caldera, which may be dominated by ice flows and snow accumulation. For landslides, ArcticDEM gives the first quantitative estimates of the total area (0.025 km²) and volume ((400 ± 8) × 10^3 m³) of the 2017 Kinnikinnick landslide in Alaska. For retrogressive thaw slumps, the topographic profile from ArcticDEM is consistent with both ICESat-2 and field measurements. ArcticDEM-derived mass losses within the scar areas of slumps are consistent with the volumes from field data. For snowdrifts, ArcticDEM strips are shown to be able to detect high-accumulation, late-lying snow areas, and seasonal snowdrift dynamics. The ArcticDEM-derived snowdrifts signal agrees well with field measurements with a standard deviation of around 0.25 m. For vegetation heights, ArcticDEM data can retrieve heights with an uncertainty of 0.33 m when a LiDAR DTM is adopted as the bare ground elevation model. The illustration of five distinct applications underscores the challenge of disentangling signals in certain geographic contexts. Common error sources within ArcticDEM data are also discussed, including large blunders from clouds, shadows, water, image saturation, tilts, along-track stripes, random noise, as well as translational offsets. The free access to ArcticDEM data allows for a wide range of applications, including and beyond those we have demonstrated, as well as upscaling field data, providing measurements in areas where collecting field data may be unsafe, and adding the vertical and time dimensions to other remote sensing analysis. The pioneer case studies demonstrated in this paper will guide the extended use of this openly accessible dataset in many disciplines. The upcoming global coverage of the time dependent DEM data (EarthDEM) will broaden the application to the global domain, largely increasing its impact on geosciences and environmental remote sensing.

CRediT authorship contribution statement

Chunli Dai: Writing – original draft, Software, Funding acquisition, Formal analysis, Data curation, Conceptualization. **Ian M. Howat:** Writing – review & editing, Resources, Formal analysis. **Jurjen van der Sluijs:** Writing – review & editing, Writing – original draft, Visualization, Validation, Formal analysis. **Anna K. Liljedahl:** Writing – review & editing, Validation, Conceptualization. **Bretwood Higman:** Writing – review & editing, Validation, Resources, Data curation. **Jeffrey T. Freymueller:** Writing – review & editing, Validation, Resources, Formal analysis, Data curation. **Melissa K. Ward Jones:** Writing – review & editing, Validation, Resources. **Steven V. Kokelj:** Writing – review & editing, Validation, Resources. **Julia Boike:** Writing – review & editing, Validation, Resources. **Branden Walker:** Writing – review & editing, Validation. **Philip Marsh:** Writing – review & editing, Validation.

Declaration of competing interest

The authors declare that they have no known competing financial interests or personal relationships that could have appeared to influence the work reported in this paper.

Data availability

The data products generated in this study including the surface elevation change maps, uncertainties, and other related shapefiles are available online (https://doi.org/10.17632/6dy5jnymww.1).

Appendix A. Supplementary data

Supplementary data to this article can be found online at https://doi.org/10.1016/j.srs.2024.100130.

References

Anders, K., Antonova, S., Boike, J., Gehrmann, M., Hartmann, J., Helm, V., Höfle, B., Marsh, P., Marx, S., Sachs, T., 2018. Airborne Laser Scanning (ALS) Point Clouds of Trail Valley Creek, NWT, Canada (2016). PANGAEA.

Antonova, Sofia, Anders, Katharina, Beck, Inga, Boike, Julia, Höfle, Bernhard, Marx, Sabrina, 2019b. Digital Elevation Model from Raw CoSSC TanDEM-X Data (2015) in the Area of Trail Valley Creek, Northwest Territories. PANGAEA, Canada. https://doi.org/10.1594/PANGAEA.902503.

Antonova, S., Thiel, C., Höfle, B., Anders, K., Helm, V., Zwieback, S., Marx, S., Boike, J., 2019a. Estimating tree height from TanDEM-X data at the northwestern Canadian treeline. Rem. Sens. Environ. 231, 111251.

Bagnardi, M., González, P.J., Hooper, A., 2016. High-resolution digital elevation model from tri-stereo Pleiades-1 satellite imagery for lava flow volume estimates at Fogo Volcano. Geophys. Res. Lett. 43 (12), 6267–6275.

Brovelli, M.A., Cannata, M., Longoni, U.M., 2004. LIDAR data filtering and DTM interpolation within GRASS. Trans. GIS 8 (2), 155–174.

Brown, R.D., Brasnett, B., 2010. Canadian Meteorological Centre (CMC) daily snow depth analysis data. Version 1 [Data Set]. NASA National Snow and Ice Data Center Distributed Active Archive Center, Boulder, Colorado USA. https://doi.org/10.5067/W9FOYWH0EQZ3. (Accessed 30 August 2022).

Corsa, B.D., Jacquemart, M., Willis, M.J., Tiampo, K.F., 2022. Characterization of large tsunamigenic landslides and their effects using digital surface models: a case study from Taan Fiord, Alaska. Rem. Sens. Environ. 270, 112881.

Dai, C., Higman, B., Lynett, P.J., Jacquemart, M., Howat, I.M., Liljedahl, A.K., Dufresne, A., Freymueller, J.T., Geertsema, M., Ward Jones, M., Haeussler, P.J., 2020b. Detection and assessment of a large and potentially tsunamigenic periglacial landslide in Barry Arm, Alaska. Geophys. Res. Lett. 47 (22), e2020GL089800.

Dai, C., Howat, I.M., 2017. Measuring lava flows with ArcticDEM: application to the 2012–2013 eruption of tolbachik, Kamchatka. Geophys. Res. Lett. 44 (24), 12–133.

Dai, C., Howat, I.M., 2018. Detection of saturation in high-resolution pushbroom satellite imagery. IEEE J. Sel. Top. Appl. Earth Obs. Rem. Sens. 11 (5), 1684–1693.

Dai, C., Durand, M., Howat, I.M., Altenau, E.H., Pavelsky, T.M., 2018. Estimating river surface elevation from ArcticDEM. Geophys. Res. Lett. 45 (7), 3107–3114.

Dai, C., Howat, I.M., Freymueller, J.T., Lu, Z., Vijay, S., Liljedahl, A.K., Jones, M.K.W., Bergstedt, H., Lev, E., 2022. Quantifying mass flows at Mt. Cleveland, Alaska between 2001 and 2020 using satellite photogrammetry. J. Volcanol. Geoth. Res. 429, 107614.

Dai, C., Howat, I.M., Freymueller, J.T., Vijay, S., Jia, Y., 2020a. Characterization of the 2008 phreatomagmatic eruption of okmok from ArcticDEM and InSAR: deposition, erosion, and deformation. J. Geophys. Res. Solid Earth 125 (6), e2019JB018977.

Derksen, C., Silis, A., Sturm, M., Holmgren, J., Liston, G.E., Huntington, H., Solie, D., 2009. Northwest Territories and Nunavut snow characteristics from a subarctic traverse: implications for passive microwave remote sensing. J. Hydrometeorol. 10 (2), 448–463.

Dirscherl, M., Rossi, C., 2018. Geomorphometric analysis of the 2014–2015 Bárðarbunga volcanic eruption, Iceland. Rem. Sens. Environ. 204, 244–259.

Dulfer, H.E., Stoker, B.J., Margold, M., Stokes, C.R., 2023. Glacial geomorphology of the northwest laurentide ice sheet on the northern interior plains and western Canadian shield, Canada. J. Maps 1–18.

Durkin, W., Kachuck, S., Pritchard, M., 2019. The importance of the inelastic and elastic structures of the crust in constraining glacial density, mass change, and isostatic adjustment from geodetic observations in Southeast Alaska. J. Geophys. Res. Solid Earth 124 (1), 1106–1119.

Farr, T.G., Rosen, P.A., Caro, E., Crippen, R., Duren, R., Hensley, S., Kobrick, M., Paller, M., Rodriguez, E., Roth, L., Seal, D., 2007. The shuttle radar topography mission. Rev. Geophys. 45 (2).

Gardelle, J., Berthier, E., Arnaud, Y., 2012. Impact of resolution and radar penetration on glacier elevation changes computed from DEM differencing. J. Glaciol. 58 (208), 419–422.

Grohmann, C.H., 2018. Evaluation of TanDEM-X DEMs on selected Brazilian sites: comparison with SRTM, ASTER GDEM and ALOS AW3D30. Rem. Sens. Environ. 212, 121–133.

Grünberg, I., Boike, J., 2019. Vegetation Map of Trail Valley Creek, Northwest Territories. Canada.

Grünberg, I., Wilcox, E.J., Zwieback, S., Marsh, P., Boíke, J., 2020. Linking tundra vegetation, snow, soil temperature, and permafrost. Biogeosciences 17 (16), 4261–4279.

Gudmundsson, M.T., Jónsdóttir, K., Hooper, A., Holohan, E.P., Halldórsson, S.A., Ófeigsson, B.G., Cesca, S., Vogfjörd, K.S., Sigmundsson, F., Högnadóttir, T., Einarsson, P., 2016. Gradual caldera collapse at Bárdarbunga volcano, Iceland, regulated by lateral magma outflow. Science 353 (6296), aaf8988.

Harder, P., Schirmer, M., Pomeroy, J., Helgason, W., 2016. Accuracy of snow depth estimation in mountain and prairie environments by an unmanned aerial vehicle. Cryosphere 10 (6), 2559–2571.

Howat, I.M., Porter, C., Smith, B.E., Noh, M.J., Morin, P., 2019. The reference elevation model of Antarctica. Cryosphere 13 (2), 665–674.

Karlson, M., Gålfalk, M., Crill, P., Bousquet, P., Saunois, M., Bastviken, D., 2019. Delineating northern peatlands using Sentinel-1 time series and terrain indices from local and regional digital elevation models. Rem. Sens. Environ. 231, 111252.

Kokelj, S.V., Lantz, T.C., Kanigan, J., Smith, S.L., Coutts, R., 2009. Origin and polycyclic behaviour of tundra thaw slumps, Mackenzie Delta region, Northwest Territories, Canada. Permafr. Periglac. Process. 20 (2), 173–184.

Kokelj, S.V., Lacelle, D., Lantz, T.C., Tunnicliffe, J., Malone, L., Clark, I.D., Chin, K.S., 2013. Thawing of massive ground ice in mega slumps drives increases in stream sediment and solute flux across a range of watershed scales. J. Geophys. Res. Earth Surf. 118 (2), 681–692.

Kokelj, S.V., Tunnicliffe, J., Lacelle, D., Lantz, T.C., Chin, K.S., Fraser, R., 2015. Increased precipitation drives mega slump development and destabilization of ice-rich permafrost terrain, northwestern Canada. Global Planet. Change 129, 56–68.

Kokelj, S.V., Tunnicliffe, J.F., Lacelle, D., 2017. The Peel Plateau of northwestern Canada: an ice-rich hummocky moraine landscape in transition. In: Landscapes and Landforms of Western Canada. Springer, Cham, pp. 109–122.

Kokelj, S.V., Kokoszka, J., van Der Sluijs, J., Rudy, A.C., Tunnicliffe, J., Shakil, S., Tank, S.E., Zolkos, S., 2021. Thaw-driven mass wasting couples slopes with

downstream systems, and effects propagate through Arctic drainage networks. Cryosphere 15 (7), 3059–3081.

Korona, J., Berthier, E., Bernard, M., Rémy, F., Thouvenot, E., 2009. SPIRIT. SPOT 5 stereoscopic survey of polar ice: reference images and topographies during the fourth International Polar Year (2007–2009). ISPRS J. Photogrammetry Remote Sens. 64 (2), 204–212.

Krieger, G., Moreira, A., Fiedler, H., Hajnsek, I., Werner, M., Younis, M., Zink, M., 2007. TanDEM-X: a satellite formation for high-resolution SAR interferometry. IEEE Trans. Geosci. Rem. Sens. 45 (11), 3317–3341.

Lacelle, D., Brooker, A., Fraser, R.H., Kokelj, S.V., 2015. Distribution and growth of thaw slumps in the Richardson Mountains–Peel Plateau region, northwestern Canada. Geomorphology 235, 40–51.

Lange, S., Grünberg, I., Anders, K., Hartmann, J., Helm, V., Boike, J., 2021. Airborne Laser Scanning (ALS) Point Clouds of Trail Valley Creek, NWT, Canada (2018). PANGAEA. https://doi.org/10.1594/PANGAEA.934387.

Li, T., Hu, Y., Liu, B., Jiang, L., Wang, H., Shen, X., 2023. Co-registration and residual correction of digital elevation models: a comparative study. Cryosphere 17 (12), 5299–5316.

Lu, X., Yang, K., Lu, Y., Gleason, C.J., Smith, L.C., Li, M., 2020. Small Arctic rivers mapped from Sentinel-2 satellite imagery and ArcticDEM. J. Hydrol. 584, 124689.

Mallory, M.L., Gilchrist, H.G., Janssen, M., Major, H.L., Merkel, F., Provencher, J.F., Strøm, H., 2018. Financial costs of conducting science in the Arctic: examples from seabird research. Arctic Science 4 (4), 624–633.

Marti, R., Gascoin, S., Berthier, E., De Pinel, M., Houet, T., Laffly, D., 2016. Mapping snow depth in open alpine terrain from stereo satellite imagery. Cryosphere 10 (4), 1361–1380.

McMartin, I., Godbout, P.M., Campbell, J.E., Tremblay, T., Behnia, P., 2021. A new map of glacigenic features and glacial landsystems in central mainland Nunavut, Canada. Boreas 50 (1), 51–75.

Meddens, A.J., Vierling, L.A., Eitel, J.U., Jennewein, J.S., White, J.C., Wulder, M.A., 2018. Developing 5 m resolution canopy height and digital terrain models from WorldView and ArcticDEM data. Rem. Sens. Environ. 218, 174–188.

Montesano, P.M., Neigh, C.S., Wagner, W., Wooten, M., Cook, B.D., 2019. Boreal canopy surfaces from spaceborne stereogrammetry. Rem. Sens. Environ. 225, 148–159.

Neigh, C.S., Masek, J.G., Bourget, P., Cook, B., Huang, C., Rishmawi, K., Zhao, F., 2014. Deciphering the precision of stereo IKONOS canopy height models for US forests with G-LiHT airborne LiDAR. Rem. Sens. 6 (3), 1762–1782.

Nitze, I., Heidler, K., Barth, S., Grosse, G., 2021. Developing and testing a deep learning approach for mapping retrogressive thaw slumps. Rem. Sens. 13 (21), 4294.

Noh, M.J., Howat, I.M., 2013. Automated coregistration of repeat digital elevation models for surface elevation change measurement using geometric constraints. IEEE Trans. Geosci. Rem. Sens. 52 (4), 2247–2260.

Noh, M.J., Howat, I.M., 2015. Automated stereo-photogrammetric DEM generation at high latitudes: surface Extraction with TIN-based Search-space Minimization (SETSM) validation and demonstration over glaciated regions. GIScience Remote Sens. 52 (2), 198–217.

Noh, M.J., Howat, I.M., 2017. The surface extraction from TIN based search-space minimization (SETSM) algorithm. ISPRS J. Photogrammetry Remote Sens. 129, 55–76.

Noh, M.J., Howat, I.M., 2019. Applications of high-resolution, cross-track, pushbroom satellite images with the SETSM algorithm. IEEE J. Sel. Top. Appl. Earth Obs. Rem. Sens. 12 (10), 3885–3899.

Nuth, C., Kääb, A., 2011. Co-registration and bias corrections of satellite elevation data sets for quantifying glacier thickness change. Cryosphere 5 (1), 271–290.

Porter, C., Morin, P., Howat, I., Noh, M.J., Bates, B., Peterman, K., Keesey, S., Schlenk, M., Gardiner, J., Tomko, K., Willis, M., Kelleher, C., Cloutier, M., Husby, E., Foga, S., Nakamura, H., Platson, M., Wethington, M., Williamson, C., Bauer, G., Enos, J., Arnold, G., Kramer, W., Becker, P., Doshi, A., D'Souza, C., Cummens, P., Laurier, F., Bojesen, M., 2018. ArcticDEM, version 3. https://doi.org/10.7910/DVN/OHHUKH. (Accessed 27 November 2023). Harvard Dataverse, V1.

Porter, Claire, Howat, Ian, Noh, Myoung-Jon, Husby, Erik, Khuvis, Samuel, Danish, Evan, Tomko, Karen, Gardiner, Judith, Negrete, Adelaide, Yadav, Bidhyananda, Klassen, James, Kelleher, Cole, Cloutier, Michael, Bakker, Jesse, Enos, Jeremy, Arnold, Galen, Bauer, Greg, Morin, Paul, 2022. "ArcticDEM – strips, version 4.1". Harvard Dataverse. https://doi.org/10.7910/DVN/C98DVS. (Accessed 3 November 2022). V1.

Porter, Claire, Howat, Ian, Noh, Myoung-Jon, Husby, Erik, Khuvis, Samuel, Danish, Evan, Tomko, Karen, Gardiner, Judith, Negrete, Adelaide, Yadav, Bidhyananda, Klassen, James, Kelleher, Cole, Cloutier, Michael, Bakker, Jesse, Enos, Jeremy, Arnold, Galen, Bauer, Greg, Morin, Paul, 2023. "ArcticDEM, version 4.1". Harvard Dataverse. https://doi.org/10.7910/DVN/3VDC4W. (Accessed 20 August 2023). V1.

Puliti, S., Hauglin, M., Breidenbach, J., Montesano, P., Neigh, C.S.R., Rahlf, J., Solberg, S., Klingenberg, T.F., Astrup, R., 2020. Modelling above-ground biomass stock over Norway using national forest inventory data with ArcticDEM and Sentinel-2 data. Rem. Sens. Environ. 236, 111501.

Rantanen, M., Karpechko, A.Y., Lipponen, A., Nordling, K., Hyvärinen, O., Ruosteenoja, K., Vihma, T., Laaksonen, A., 2022. The Arctic has warmed nearly four times faster than the globe since 1979. Communications Earth & Environment 3 (1), 168.

Reynolds, H.I., Gudmundsson, M.T., Högnadóttir, T., Magnússon, E., Pálsson, F., 2017. Subglacial volcanic activity above a lateral dyke path during the 2014–2015 Bárðarbunga-Holuhraun rifting episode, Iceland. Bull. Volcanol. 79 (6), 1–13.

Reynolds, H.I., Gudmundsson, M.T., Högnadóttir, T., Axelsson, G., 2019. Changes in geothermal activity at Bárðarbunga, Iceland, Following the 2014–2015 caldera collapse, Investigated using geothermal system modeling. J. Geophys. Res. Solid Earth 124 (8), 8187–8204.

RGI Consortium, 2017. Randolph Glacier inventory – a dataset of global glacier outlines: version 6.0: technical report, global land ice measurements from space, Colorado, USA. Digit. Media. https://doi.org/10.7265/N5-RGI-60.

Rixen, C., Høye, T.T., Macek, P., Aerts, R., Alatalo, J.M., Anderson, J.T., Arnold, P.A., Barrio, I.C., Bjerke, J.W., Björkman, M.P., Blok, D., 2022. Winters are changing: snow effects on Arctic and alpine tundra ecosystems. Arctic Science 8 (3), 572–608.

Rossi, C., Minet, C., Fritz, T., Eineder, M., Bamler, R., 2016. Temporal monitoring of subglacial volcanoes with TanDEM-X—application to the 2014–2015 eruption within the Bárðarbunga volcanic system, Iceland. Rem. Sens. Environ. 181, 186–197.

Runge, A., Nitze, I., Grosse, G., 2022. Remote sensing annual dynamics of rapid permafrost thaw disturbances with LandTrendr. Rem. Sens. Environ. 268, 112752.

Shean, D.E., Alexandrov, O., Moratto, Z.M., Smith, B.E., Joughin, I.R., Porter, C., Morin, P., 2016. An automated, open-source pipeline for mass production of digital elevation models (DEMs) from very-high-resolution commercial stereo satellite imagery. ISPRS J. Photogrammetry Remote Sens. 116, 101–117.

Shean, D.E., Joughin, I.R., Dutrieux, P., Smith, B.E., Berthier, E., 2019. Ice shelf basal melt rates from a high-resolution digital elevation model (DEM) record for Pine Island Glacier, Antarctica. Cryosphere 13 (10), 2633–2656.

Shiggins, C.J., Lea, J.M., Brough, S., 2023. Automated ArcticDEM iceberg detection tool: insights into area and volume distributions, and their potential application to satellite imagery and modelling of glacier–iceberg–ocean systems. Cryosphere 17 (1), 15–32.

Sigmundsson, F., Hooper, A., Hreinsdóttir, S., Vogfjörd, K.S., Ófeigsson, B.G., Heimisson, E.R., Dumont, S., Parks, M., Spaans, K., Gudmundsson, G.B., Drouin, V., 2015. Segmented lateral dyke growth in a rifting event at Bárðarbunga volcanic system, Iceland. Nature 517 (7533), 191–195.

Van der Sluijs, J., Kokelj, S.V., Fraser, R.H., Tunnicliffe, J., Lacelle, D., 2018. Permafrost terrain dynamics and infrastructure impacts revealed by UAV photogrammetry and thermal imaging. Rem. Sens. 10 (11), 1734.

Smith, B., Adusumilli, S., Csathó, B.M., Felikson, D., Fricker, H.A., Gardner, A., Holschuh, N., Lee, J., Nilsson, J., Paolo, F.S., Siegfried, M.R., Sutterley, T., the ICESat-2 Science Team, 2021. ATLAS/ICESat-2 L3A Land Ice Height, Version 5. NASA National Snow and Ice Data Center Distributed Active Archive Center, Boulder, Colorado USA. https://doi.org/10.5067/ATLAS/ATL06.005 [Data Set]. (Accessed 23 October 2022).

Vander Jagt, B., Lucieer, A., Wallace, L., Turner, D., Durand, M., 2015. Snow depth retrieval with UAS using photogrammetric techniques. Geosciences 5 (3), 264–285.

Walker, B., Wilcox, E.J., Marsh, P., 2020. Accuracy assessment of late winter snow depth mapping for tundra environments using Structure-from-Motion photogrammetry. Arctic Science 7 (3), 588–604.

Walker, B., Wilcox, E.J., Marsh, P., 2020b. Structure-from-Motion Snow Depth Products and in Situ Observations for Late-Winter Tundra Mapping Project. Trail Valley Creek Research Station, Spring 2018. https://doi.org/10.5683/SP2/PWSKKG. Scholars Portal Dataverse.

Ward Jones, M.K., Pollard, W.H., 2021. Daily field observations of retrogressive thaw slump dynamics in the Canadian high Arctic. Arctic 74 (3), 339–354.

Ward Jones, M.K., Pollard, W.H., Jones, B.M., 2019. Rapid initialization of retrogressive thaw slumps in the Canadian high Arctic and their response to climate and terrain factors. Environ. Res. Lett. 14 (5), 055006.

Wessel, P., Smith, W.H., 1991. Free software helps map and display data. *Eos*. Transactions American Geophysical Union 72 (41), 441–446.

Witt, T., Walter, T.R., Müller, D., Guðmundsson, M.T., Schöpa, A., 2018. The relationship between lava fountaining and vent morphology for the 2014–2015 Holuhraun eruption, Iceland, analyzed by video monitoring and topographic mapping. Front. Earth Sci. 6, 235.

Woods, J., Donaldson, C., White, R.S., Caudron, C., Brandsdóttir, B., Hudson, T.S., Ágústsdóttir, T., 2018. Long-period seismicity reveals magma pathways above a laterally propagating dyke during the 2014–15 Bárðarbunga rifting event, Iceland. Earth Planet Sci. Lett. 490, 216–229.

Yin, T., Montesano, P.M., Cook, B.D., Chavanon, E., Neigh, C.S., Shean, D., Peng, D., Lauret, N., Mkaouar, A., Morton, D.C., Regaieg, O., 2023a. Modeling forest canopy surface retrievals using very high-resolution spaceborne stereogrammetry:(I) methods and comparisons with actual data. Rem. Sens. Environ. 298, 113825.

Yin, T., Montesano, P.M., Cook, B.D., Chavanon, E., Neigh, C.S., Shean, D., Peng, D., Lauret, N., Mkaouar, A., Regaieg, O., Zhen, Z., 2023b. Modeling forest canopy surface retrievals using very high-resolution spaceborne stereogrammetry:(II) optimizing acquisition configurations. Rem. Sens. Environ. 298, 113824.

Zhang, T., Liu, D., 2021. Evaluating the representative canopy surface of Arcticdem in Boreal forests. In: 2021 IEEE International Geoscience and Remote Sensing Symposium IGARSS. IEEE, pp. 6700–6703.

Zheng, W., Pritchard, M.E., Willis, M.J., Tepes, P., Gourmelen, N., Benham, T.J., Dowdeswell, J.A., 2018. Accelerating glacier mass loss on Franz Josef land, Russian Arctic. Rem. Sens. Environ. 211, 357–375.

Zwieback, S., Kokelj, S.V., Günther, F., Boike, J., Grosse, G., Hajnsek, I., 2018. Sub-seasonal thaw slump mass wasting is not consistently energy limited at the landscape scale. Cryosphere 12 (2), 549–564.

van der Sluijs, J., Kokelj, S. V., and Tunnicliffe, J. F.: Allometric scaling of retrogressive thaw slumps, The Cryosphere, 17, 4511–4533, https://doi.org/10.5194/tc-17-4511-2023, 2023.